

# Bottom-up approach for the low-cost synthesis of graphene- alumina nanosheet interfaces using bimetallic alloys

Luca Omiciuolo<sup>1</sup>, Eduardo R. Hernández<sup>2</sup>, Elisa Miniussi<sup>1</sup>, Fabrizio Orlando<sup>1</sup>, Paolo Lacovig<sup>3</sup>,  
Silvano Lizzit<sup>3</sup>, Rosanna Larciprete<sup>4</sup>, Marco Bianchi<sup>5</sup>, Søren Ulstrup<sup>5</sup>, Philip Hofmann<sup>5</sup>, Dario  
Alfè<sup>6,7</sup>, and Alessandro Baraldi<sup>1,8</sup>

<sup>1</sup>Physics Department, University of Trieste, Via Valerio 2, 34127 Trieste, Italy

<sup>2</sup>Instituto de Ciencia de Materiales de Madrid (ICMM-CSIC), Campus de Cantoblanco, 28049  
Madrid, Spain

<sup>3</sup>Elettra-Sincrotrone Trieste S.C.p.A., S.S. 14 Km 163.5, 34149 Trieste, Italy

<sup>4</sup>CNR, Institute for Complex Systems, Via Fosso del Cavaliere 100, 00133 Roma, Italy

<sup>5</sup>Department of Physics and Astronomy, Interdisciplinary Nanoscience Center, Aarhus University,  
8000 Aarhus C, Denmark

<sup>6</sup>Department of Earth Sciences, Department of Physics and Astronomy, TYC@UCL, and London  
Centre for Nanotechnology,

University College London, Gower Street, London WC1E 6BT, United Kingdom

<sup>7</sup>IOM-CNR, DEMOCRITOS National Simulation Centre, I-34100 Trieste, Italy

<sup>8</sup>IOM-CNR, Laboratorio TASC, S.S. 14 Km 163.5, I-34149 Trieste, Italy

## Abstract

**The production of high-quality graphene-oxide interfaces is normally achieved either by graphene growth via chemical vapor deposition on a metallic surface, followed by transfer of the C layer onto the oxide or by atomic layer and physical vapour deposition of the oxide on graphene. Both methods, however, come with a series of issues: they are complex, costly and can easily result in damage to the carbon network by introducing defects and contaminants with detrimental effects on the carrier mobility. Here we show that the epitaxial growth of a graphene layer on a bimetallic Ni<sub>3</sub>Al alloy and its subsequent exposure to oxygen at 520 K result in the selective oxidation of the Al atoms and in the formation of a 1.5 nm thick alumina nanosheet underneath graphene. This new, simple and low-cost strategy based on the use of alloys opens a promising route to the direct synthesis of a wide range of interfaces formed by graphene and high- $\kappa$  dielectrics.**

The coupling of graphene (GR) with 2D nanosheet dielectrics<sup>1-4</sup> is an important topic in contemporary materials science, due to its potential impact on a number of high-performance nanoelectronic applications<sup>5</sup>. In this respect, Al<sub>2</sub>O<sub>3</sub> films play a key role because of their employment as high- $\kappa$  oxides in transistors and low-power chips, where the use of a high dielectric constant ( $\epsilon_r = 9$ )<sup>6</sup> increases the gate capacitance. Recent studies have reported a high mobility of exfoliated GR in Al<sub>2</sub>O<sub>3</sub>/GR interfaces synthesised using alumina nanoribbons (23600 cm<sup>2</sup>/V·s)<sup>7</sup> or ozone functionalization methods (19000 cm<sup>2</sup>/V·s)<sup>8</sup>.

However, the conventional methods so far used for producing GR-alumina interfaces inevitably lead to a degradation of the electronic properties of GR. Chemical vapour deposition (CVD) growth on transition metals<sup>2</sup> requires a transfer process involving the use of polymers, solvents, and etchants/water solutions which introduce contaminants or defects<sup>9</sup>, such as vacancies, grain boundaries, and GR multilayers. On the other hand, atomic layer deposition (ALD), used to directly synthesise oxide layers on top of GR, typically requires a chemical modification of GR to avoid

wetting problems, and introduces impurities or causes C-C bond cleavages, leading to a significant degradation of the electron mobility. More recent alternative strategies, based on Hf and Si deposition and subsequent oxidation, have always been adopted in combination with expensive transition metal supports, such as Pt<sup>10</sup> and Ru<sup>11</sup>. It is therefore desirable to develop some simple, scalable, and economically affordable methods for the transfer-free production of GR-dielectric interfaces.

Starting from a clean Ni<sub>3</sub>Al(111) surface (Fig. 1(a)), we here propose a novel approach for the direct synthesis of GR-alumina interfaces, by growing GR on the substrate by ethylene CVD (Fig. 1(b)) and subsequently oxidizing the metallic surface, in such a way as to induce the formation of an alumina nanosheet (Fig. 1(c)). This method, based on the use of low cost raw materials such as NiAl, could be readily extended also to other alloys to produce high- $\kappa$  dielectrics.

## Results

A graphene layer was first grown on Ni<sub>3</sub>Al(111) by ethylene CVD at 950 K, similar to the procedure used for the growth on Ni(111)<sup>12</sup> (see Supplementary Information). The first direct evidence of GR formation on Ni<sub>3</sub>Al(111) comes from the C 1s core level spectrum, presented in Fig. 2 (a). At low exposure we observe a peak at about 283.5 eV binding energy, most probably due to C<sub>2</sub>H<sub>4</sub> fragments and carbides, while at higher carbon coverage a new component appears at higher binding energy (284.84 eV), attributed to GR by comparison with GR on Ni(111)<sup>13</sup>. The integrated intensity of this peak shows a saturating behaviour, indicating a self-limiting growth process. The high-energy resolution C 1s core level spectrum measured at room temperature reveals two narrow components separated by 410 meV (higher BE component at 284.84 eV).

The corresponding fast XPS measurements of the Al 2p core level clearly is consistent with the presence of a GR layer (Fig. 2 (b)), which causes a ~65% reduction of the Al 2p integrated intensity. The high-resolution Al 2p spectrum of GR-covered Ni<sub>3</sub>Al, compared with that of the clean sample (shown superimposed in Fig. 2 (b)), shows an additional spin-orbit doublet (green components),

shifted by +160 meV, which is assigned to the interacting Al atoms at the metal-GR interface.

The low energy electron diffraction pattern of the GR/Ni<sub>3</sub>Al(111) interface, reported in Fig. 2 (c), shows the same (2x2) hexagonal periodicity as observed for the clean substrate<sup>14</sup> (shown as green circles in Fig. 2 (c)), indicating that the first bimetallic layer, which presents a lattice mismatch of only 2.4 % with respect to GR, has not undergone any reconstruction or structural modification. Some differences relative to the clean case can be discernible, in particular, a very weak ring-shaped modulation reflecting the presence of residual differently oriented GR domains, as previously reported for Ni(111)<sup>15</sup>.

To get a more detailed insight into the structure and properties of the GR/Ni<sub>3</sub>Al system, we have performed DFT calculations for six possible high-symmetry configurations obtained by imposing the constraint of GR forming a (2x2) superstructure on Ni<sub>3</sub>Al(111) (see Supplementary Information). In particular, we focused our attention on the top-fcc, top-hcp, fcc-hcp, b-top, b-fcc and b-hcp structures, i.e. corresponding to structures having carbon atoms in different adsorption sites relative to the Ni substrate atoms. We found that the minimum energy configuration is the b-top, followed by the top-fcc (Fig. 2 (d)), separated by only 60 meV, similarly to what was obtained in DFT calculations of GR on Ni(111)<sup>16</sup>. The b-fcc and b-hcp are not stable and relax into a top-fcc and top-hcp structure, respectively. Finally, the top-hcp and fcc-hcp configurations turn out to be the least stable, with a significantly higher energy.

Angle-resolved photoemission (ARPES) measurements (Fig. 2 (e) and (f)) show the disruption of the Dirac cone, with the whole  $\pi$ -band of the GR layer shifted to higher binding energy with respect to free-standing GR. This is similar to what has been reported for GR on Ni(111)<sup>12</sup> and results from the strong hybridization between GR and metal 3d valence band states. In particular the bottom of the band, at the M point, is found at  $\sim 4.7$  eV below the Fermi level, while the Dirac point is found at  $\sim 2.7$  eV. The high density of states at the Fermi level ( $E_F$ ), instead, is mainly due to the Ni d-band of the alloy substrate. The calculated band structure for the top-fcc GR-Ni<sub>3</sub>Al(111) geometry (Fig. 2 (g)), shows an excellent agreement with the experimental data, supporting the hypothesis that the

observed structure is predominantly top-fcc.

To further understand which of the two minimum energy structures corresponds to the experimentally observed one, we calculated the C 1s core electron binding energies for all the non-equivalent carbon atoms (see Supplementary Information). By comparing the simulated photoemission spectrum for the two cases, we found a better agreement for the top-fcc structure, as reported in the top panel of Fig. 2 (a) (red line). However, the coexistence of the two phases cannot be excluded. Finally, for the top-fcc structure, the calculated mean distance between the GR layer and the substrate is 2.12 Å, similar to the GR-Ni(111) system<sup>16</sup>.

After GR growth, the GR-alloy interface was exposed to a high flux of molecular oxygen ( $p=3\cdot 10^{-3}$  torr) at 520 K. Following this procedure, it is possible to intercalate oxygen underneath the GR layer and to selectively oxidize only the Al atoms at the metal interface. In fact, the intercalation of noble or light atoms has already proven to be an effective method to create an interface nanosheet between GR and the substrate<sup>17-20</sup>.

Fig. 3 (a) and (b) show a set of high-resolution photoemission spectra acquired after different oxygen exposures, for the C 1s and Al 2p levels, respectively. Looking at the C 1s spectrum, we observe the appearance of a new component at lower binding energy with respect to the previously described GR peak. From a comparison of our data with previous literature<sup>11,21</sup>, we ascribe this new component to regions of GR sitting on an oxide substrate. As the oxygen dose increases, this new peak grows in intensity at the expense of the previous one, indicating that the oxide layer formation proceeds through the progressive expansion of nucleation islands. Finally, above  $10^7$  L of oxygen exposure ( $1L = 1\cdot 10^{-6}$  torr·s), the signal associated with GR/NiAl basically disappears from the spectrum. After the carbon layer has been completely decoupled from the substrate, the C 1s spectrum shows a single, narrow component centred at 284.2 eV, which, notably, is shifted by ~590 meV to lower binding energy with respect to the higher binding energy C 1s components ( $C_0$ ) of GR/Ni<sub>3</sub>Al(111). It is important to note that, during the intercalation process, the total C 1s intensity decreases by less than 5%, indicating that the overall integrity of the carbon network is preserved.

The selective oxidation of the Al atoms in the first few layers was monitored by following the evolution of the Al 2p core level spectra acquired at increasing oxygen exposure (Fig. 2 (b)). As oxygen intercalation proceeds, we observe the growth of a broad peak, centred at about 73.8 eV, in the same binding energy region as the signal that typically accompanies the formation of an alumina film on NiAl alloys<sup>22</sup>.

On the other hand, as it is clear from the evolution of the Ni 2p<sub>3/2</sub> spectra, the Ni atoms are almost unaffected by the oxidation process. This finding can be explained in terms of a thermally promoted surface segregation of the Al atoms, resulting in a Ni-depleted first layer. Since the oxide layer is mainly formed by alumina, we were able to estimate the oxide layer thickness from the intensity decrease of the Ni 2p<sub>3/2</sub> signal. The estimated mean thickness of the alumina layer, taking into account the inelastic photoelectron mean free path, is  $\sim 1.5 \pm 0.2$  nm.

The DFT calculated structure for a GR layer on the Al<sub>2</sub>O<sub>3</sub> (0001)  $\alpha$ -phase (Fig. 3 (c)), which approximately reproduces the experimentally obtained thick alumina layer (see methods), shows a distance of 2.85 Å between GR and the oxide substrate.

The ARPES measurements, reported in Fig. 3 (d), show that the Dirac cone in the vicinity of the Fermi energy is fully restored, thus confirming that GR is sitting on top of 1.5 nm thick oxide layer which effectively decouples it from the metallic alloy. In particular, the bottom of the  $\pi$  band located at the M point, shifts by about 2 eV, with the Dirac point lying above the Fermi energy. Moreover, close to the K and K' points, the energy dispersion becomes linear, as expected for quasi-free-standing GR. From a linear fit of the dispersion curve close to the K point, we estimated that the group velocity of the charge carriers ( $dE(k)/dk$ ) is  $\sim 8 \cdot 10^5$  m/s ( $\sim 1/370$  of the speed of light), in good agreement with the theoretically predicted value for free-standing GR. From a linear extrapolation, we estimated that the Dirac point is  $200 \pm 40$  meV above  $E_F$ , thus indicating an oxide-induced p-doping of the GR layer. The DFT calculated electronic dispersion shows an excellent agreement with the experimental data. In particular, the bottom of the  $\pi$ -band and the region near the Dirac point are well reproduced (Fig. 3 (e)). The calculated band energy value at the

K point lies 220 meV below  $E_F$ , consistent with the experimental value.

In order to understand the effect of the GR layer after the substrate oxidation in comparison to the clean surface, we have performed a series of oxidation experiments on the bare  $\text{Ni}_3\text{Al}(111)$ . Fig. 4 shows a set of photoemission spectra of the clean and GR-covered sample measured under similar oxygen coverage conditions. The Al 2p spectra measured before and after GR growth are reported in Fig. 4 (a). The clean  $\text{Ni}_3\text{Al}$  crystal was first exposed to an  $\text{O}_2$  pressure of  $4 \cdot 10^{-7}$  torr at 520 K, up to approximately the same coverage as reached in the oxygen intercalation experiment (Fig. 4). After oxidation, the Al 2p spectrum is comparable to the one obtained in the presence of GR, apart from an intensity enhancement due to the absence of the carbon layer. In particular, both spectra show a broad peak centered at the same binding energy (73.8 eV), while a residual signal arising from the metallic Al atoms is still present. This suggests that oxygen intercalation on the GR-covered sample at 520 K leads to the formation of an oxide layer with the same composition to the one obtained upon oxidation of the clean substrate. Notably, the effect of GR on the Al 2p signal reduction amounts to 65% in both cases. Our findings suggest that the presence of the GR layer plays a minor role in the oxide layer structure.

## Discussion

Besides its simplicity, the method we have developed offers the advantage of using low cost raw materials, which can be easily processed by conventional metal powder technology. Our method could be used also with other Al-based bimetallic alloys ( $\text{CuAl}_2$ ,  $\text{CoAl}$ ,  $\text{FeAl}$ ,  $\text{Fe}_3\text{Al}$ ) capable of breaking the C-H bonds in hydrocarbon molecules and to selectively oxidize the Al atoms. The availability of a large range of low-cost bimetallic compounds ( $\text{NiZr}$ ,  $\text{NiTi}$ , etc) can open new avenues for GR integrated materials with higher dielectric constant ( $\text{ZrO}_2$   $\epsilon_r = 25$ ,  $\text{TiO}_2$   $\epsilon_r = 30$  (anatase)-100 (rutile), etc)) than conventional  $\text{SiO}_2$  ( $\epsilon_r = 3.9$ ). The coupling of GR with oxide nanosheets could be also exploited in spin-filtering materials, to remove the spin-scattering effects arising when the GR layer is directly supported on transition metals. The thickness of the so-

produced oxide layer is comparable to the values used in the latest high-efficient spin transport devices. Finally, other oxide layers could be deposited, by means of well-established methods, on top of the GR-oxide interface, in such a way to build oxide-GR-oxide sandwiched heterostructures, which represents a fundamental architecture in most new generation electronic devices.

## Methods

The Ni<sub>3</sub>Al (111) single crystal used in this work was polished before the experiment, then cleaned in UHV conditions by repeated cycles of 2 keV Ar<sup>+</sup> sputtering and annealing to 1170 K. This procedure ensured a high quality surface, as judged by LEED and XPS. The measurements reported in this work were also performed in UHV conditions, with a background pressure of the order of  $1 \cdot 10^{-10}$  torr.

The high-energy resolution XPS and fast XPS experiments were carried out at the SuperESCA undulator beamline of the Elettra synchrotron radiation facility (Basovizza – Italy). The photoemitted electrons were collected and analyzed by a state-of-the-art SPECS PHOIBOS 150 hemispherical analyzer equipped with a delay line detector developed at Elettra. The C 1s, Al 2p, Ni 2p<sub>3/2</sub> and O 1s spectra with their corresponding Fermi levels were acquired with a photon energy of 400 eV, 230 eV, 950 eV and 650 eV, respectively. All the spectra were measured in normal emission geometry. A linear background was always subtracted from the core level signal, except for the Ni 2p<sub>3/2</sub> spectra, for which a Shirley-type background was instead used. The spectra were then re-offset to the corresponding Fermi energies and fitted to a multipeak Doniach-Šunjić function convoluted with a Gaussian.

The ARPES measurements were performed at the SGM3 undulator beamline of the ASTRID storage ring in Aarhus (Denmark). The two-dimensional detector, consisting of a phosphor screen coupled with a high resolution CCD camera, combined with a PHOIBOS 150 hemispherical analyzer, yields an angular resolution better than 0.15° and an energy resolution of the order of 10 meV. The angle resolved spectra were acquired with a photon energy of 50 eV. The LEED patterns were acquired with a standard LEED system both at the SuperESCA and at the SGM3 beamlines.

The Density Functional Theory (DFT)<sup>23,24</sup> calculations were performed with the VASP code<sup>25</sup>. We employed a plane-wave basis set including all plane waves up to a kinetic energy of 400 eV, and the core electrons were treated with the Projector Augmented Wave (PAW) method<sup>26</sup> as implemented in VASP<sup>26</sup>. Spin-polarized calculations were performed with several different functionals, among

which we included the LDA, PBE<sup>28</sup>, Grimme<sup>29</sup> and Dion et al.<sup>30</sup> functionals (see below). A 2x2 slab of Ni<sub>3</sub>Al (111) containing 18 Ni atoms and 6 Al atoms (a total of six layers) was employed to simulate the surface, with a vacuum region above the slab of approximately 16.5 Å. The three bottom layers were frozen in their atomic bulk positions, while the remaining layers were allowed to relax. The structural relaxation was performed using the conjugate gradients algorithm. Once the slab geometry had been optimized, a 2x2 GR supercell formed by 8 C atoms was placed on top of it in various configurations, as discussed in the text, and the resulting structures were relaxed once again. The same procedure was used to simulate GR on the  $\alpha$ -phase of Al<sub>2</sub>O<sub>3</sub> (0001). In this case the slab consisted of 12 Al atoms and 18 O atoms. Apart from this, the calculations were carried out in the same way as for the Ni<sub>3</sub>Al-GR case.

Our relaxation calculations with the various exchange-correlation functionals revealed that both the PBE and Dion et al. functionals find no favourable interaction between GR and the Ni<sub>3</sub>Al substrate, in open contradiction with the experimental results. In contrast, the LDA and Grimme functionals provide very consistent results, indicating that the bridge-top is the most favorable structure, closely followed by the top-fcc arrangement, which was predicted to be 0.06 eV less stable (meaning a difference of less than 0.01 eV/C atom). All subsequent calculations were thus performed with the LDA functional.

The core electron binding energies were calculated in the final-state approximation: first a standard calculation was performed on the fully relaxed system. Then an electron from the selected core level of the atom under consideration was excited into the lowest conduction state, and the electronic structure re-calculated at fixed atomic positions. The difference between these two energies serves as an estimate of the initial core level binding energy.

## References

- [1] Novoselov, K. S. *et al.*, A roadmap for graphene. *Nature* **490**, 192 (2012).
- [2] Batzill, M., The surface science of graphene: metal interfaces, CVD synthesis, nanoribbons, chemical modifications, and defects. *Surf. Sci. Rep.* **67**, 83 (2012).
- [3] Wang, X. -R., Tabakman, S. M., Scott M., & Dai, H. J., Atomic layer deposition of metal oxides on pristine and functionalized graphene. *J. Am. Chem. Soc.* **130**, 8152 (2008)
- [4] Gao, L., *et al.*, Face-to-face transfer of wafer-scale graphene films. *Nature* **505**, 190 (2014)
- [5] Osada, M., Sasaki, T., Two-dimensional dielectric nanosheets: novel nanoelectronics from nanocrystal building blocks. *Advan. Mater.* **24**, 21 (2012).
- [6] Colombo, L., Wallace, R. M., & Ruoff, R. S., Graphene growth and device integration. *Proc. IEEE* **101**, 1536 (2013).
- [7] Lei Liao, L., *et al.*, High- $\kappa$  oxide nanoribbons as gate dielectrics for high mobility top-gated graphene transistors. *Proc. Natl. Acad. Sci. USA* **107**, 6711 (2010)
- [8] Jandhyala, S., *et al.*, Atomic layer deposition of dielectrics on graphene using reversibly physisorbed ozone. *ACS Nano* **6**, 2722 (2012).
- [9] Hashimoto, A., Suenaga, K., Gloter, A., Urita, K., & Iijima, S., Direct evidence for atomic defects in graphene layers. *Nature* **870**, 430 (2004).
- [10] Addou, R., Dahal, A. & Batzill, M. Growth of a two-dimensional dielectric monolayer on quasi-freestanding graphene. *Nature Nanotech.* **8**, 41 (2013)
- [11] Lizzit, S. *et al.*, Transfer-free electrical insulation of epitaxial graphene from its metal substrate. *Nano Lett.* **12**, 4503 (2012).
- [12] Varykhalov, A. *et al.*, Electronic and magnetic properties of quasi-free-standing graphene on Ni. *Phys. Rev. Lett.* **101**, 157601 (2008).
- [13] Patera, L. L. *et al.*, In situ observations of the atomistic mechanisms of Ni catalyzed low temperature graphene growth. *ACS Nano* **7**, 7901 (2013)

- [14] Vesselli, E. *et al.*, The Ni<sub>3</sub>Al(111) surface structure: experiment and theory. *J. Phys.: Cond. Matt.* **20**, 195223 (2008)
- [15] Zhao, W. *et al.*, Graphene on Ni(111): coexistence of different surface structure. *J. Phys. Chem. Lett.* **2**, 759 (2011).
- [16] Mittendorfer, F. *et al.*, Graphene on Ni(111): strong interaction and weak adsorption. *Phys. Rev. B* **84**, 201401 (2012).
- [17] Sutter, P., Sadowski, J. T., & Sutter, E. A., Chemistry under cover: tuning metal-graphene interaction by reactive intercalation. *J. Am. Chem. Soc.* **132**, 8175 (2010).
- [18] Larciprete, R. *et al.* Oxygen switching of the epitaxial graphene-metal interaction. *ACS Nano* **6**, 9551 (2012).
- [19] Riedl, C., Coletti, C., Iwasaki, T., Zakharov, A. A. & Starke, U., Quasi-free-standing epitaxial graphene on SiC obtained by hydrogen intercalation. *Phys. Rev. Lett.* **103**, 246804 (2009).
- [20] Shikin, A.M., Prudnikova, G. V., Adamchuk, V. K., Moresco, F. & Rieder, K. -H. Surface intercalation of gold underneath a graphite monolayer on Ni(111) studied by angle-resolved photoemission and high-resolution electron-energy-loss spectroscopy. *Phys. Rev. B* **62**, 13202 (2000).
- [21] Preobrajenski, A. B., Ng, M. L., Vinogradov, A. S. & Mårtensson, N., Controlling graphene corrugation on lattice-mismatched substrates. *Phys. Rev. B* **78**, 073401 (2008).
- [22] Vesselli, E., Baraldi, A., Lizzit, S. & Comelli, G., Large interlayer relaxation at a metal-oxide interface: the case of a supported ultrathin alumina film. *Phys. Rev. Lett.* **105**, 046102 (2010).
- [23] Hohenberg, P. and Khon, W., Inhomogeneous electron gas. *Phys. Rev.* **136**, 864 (1964).
- [24] Kohn, W. and Sham, J. J., Self-consistent equations including exchange and correlation effects. *Phys. Rev.* **140**, 1133 (1965).
- [25] Kresse, G. and Furthmüller, J., Efficient iterative schemes for ab initio total-energy calculations

using a plane-wave basis set. *Phys. Rev. B* **54**, 11169 (1996).

[26] Blöchl, P., Projector augmented-wave method. *Phys. Rev. B* **50**, 17953 (1994).

[27] Kresse, G. & Joubert, D., From ultrasoft pseudopotentials to the projector augmented-wave method. *Phys. Rev. B* **59**, 1758 (1999).

[28] Perdew, J. P., Burke, K. & Ernzerhof, M., Generalized gradient approximation made simple. *Phys. Rev. Lett.* **77**, 3865 (1996).

[29] Grimme, S., Semiempirical GGA-type density functional constructed with a long-range dispersion correction. *J. Comput. Chem.* **27**, 1787 (2006).

[30] Dion, M., Rydberg, H., Schroder, E., Langreth, D. C. & Lundqvist, B. I., Van der Waals density functional for general geometries. *Phys. Rev. Lett.* **92**, 246401 (2004).

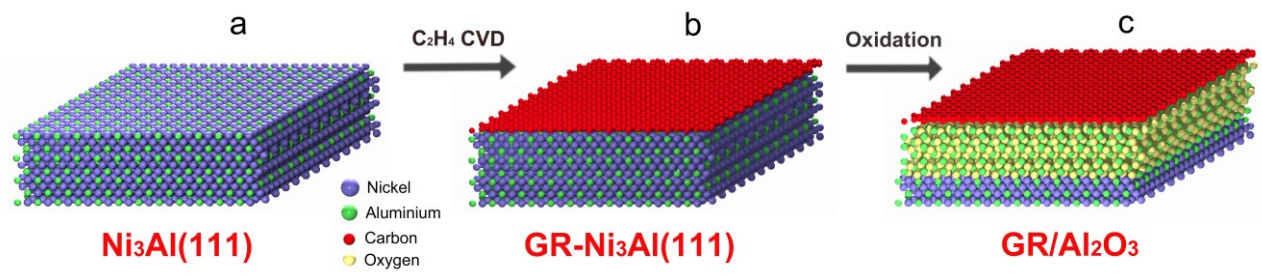


**Figure 1 | Schematic outline of the present work. (a)** The clean Ni<sub>3</sub>Al(111) surface, **(b)** GR growth on Ni<sub>3</sub>Al(111) by means of high temperature ethylene CVD, and **(c)** oxidation of the Al atoms.

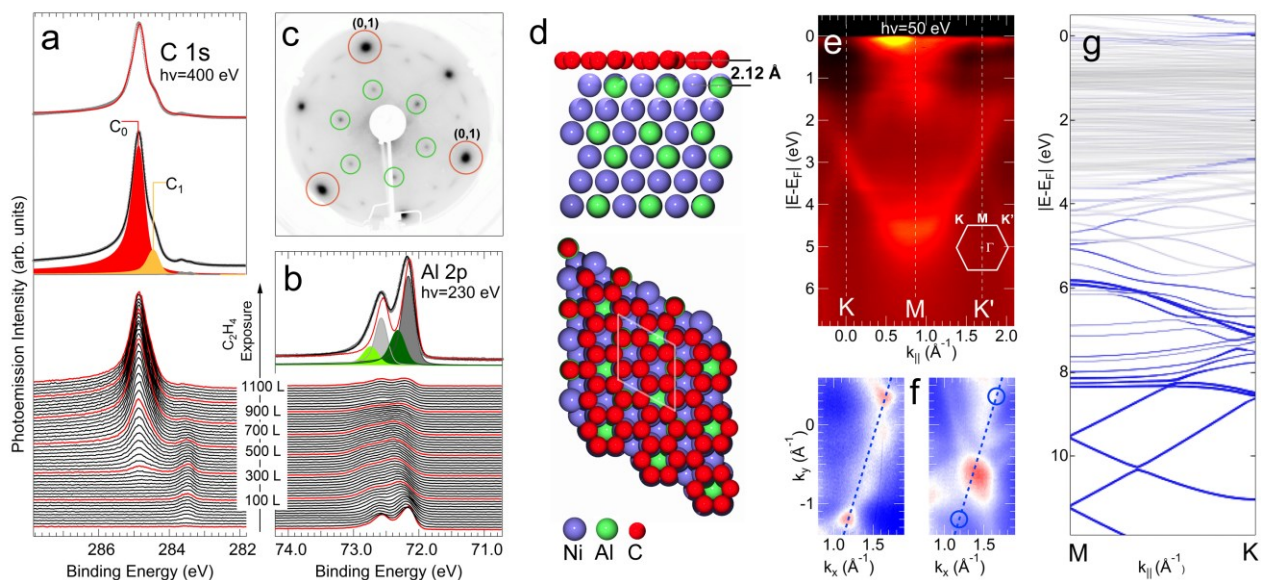


**Figure 2 | GR on Ni<sub>3</sub>Al(111).** (a) (bottom) C 1s core level photoemission spectra acquired at different exposures during ethylene CVD at 950 K. (middle) High resolution C 1s core level spectrum measured at room temperature after GR growth. The fit (black curve) and the C<sub>0</sub> (red) and C<sub>1</sub> (yellow) components are shown superimposed to the experimental data (gray circles). (top) Simulated C 1s photoemission spectrum (red line) obtained from the DFT calculated binding energies for the top-fcc structure. (b) (bottom) Al 2p core level photoemission spectra acquired at different exposures during ethylene uptake at 950 K. (top) High resolution Al 2p photoemission spectrum measured at room temperature after GR growth. The fit (black curve) is shown superimposed to the experimental data (gray circles), along with the bulk (dark/light grey) and interface (dark/light green) components for the 2p<sub>3/2</sub> and 2p<sub>1/2</sub> sublevels. The Al 2p spectrum obtained for the clean surface (red line) is plotted, after proper normalization, as a reference. (c) LEED pattern for the GR/Ni<sub>3</sub>Al(111) system measured at 150 eV. (d) Top and side views for the top-fcc GR/Ni<sub>3</sub>Al(111) structure. (e) ARPES measurement of the GR/Ni<sub>3</sub>Al(111) energy band dispersion along the K-M-K' direction in the reciprocal space and (f) constant energy surfaces at the Dirac point energy (left) and at the Fermi level (right). (g) DFT calculated GR energy band dispersion along the M-K direction for the top-fcc structure. The bands with a participation of 50% or more of carbon orbitals are highlight using blue lines.

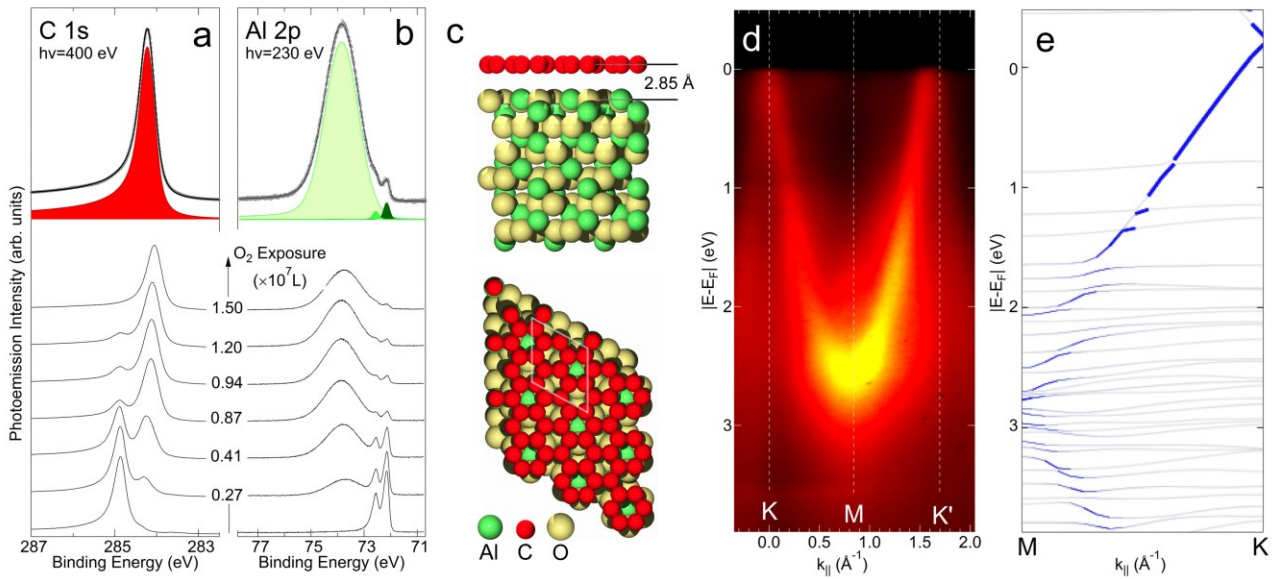


**Figure 3 | Oxygen intercalation underneath GR.** (a-b) (bottom) C 1s and Al 2p photoemission spectra acquired at different O<sub>2</sub> exposure. (top) C 1s and Al 2p high resolution spectra acquired after the formation of a thick alumina nanosheet underneath GR, the fit components are shown superimposed to the experimental data. (c) Top and side views of the simulated GR/Al<sub>2</sub>O<sub>3</sub> structure. (d) ARPES measurement of the GR/Al<sub>2</sub>O<sub>3</sub> electronic band structure along the K-M-K' direction. (e) DFT calculated energy band dispersion for the GR/Al<sub>2</sub>O<sub>3</sub> system.

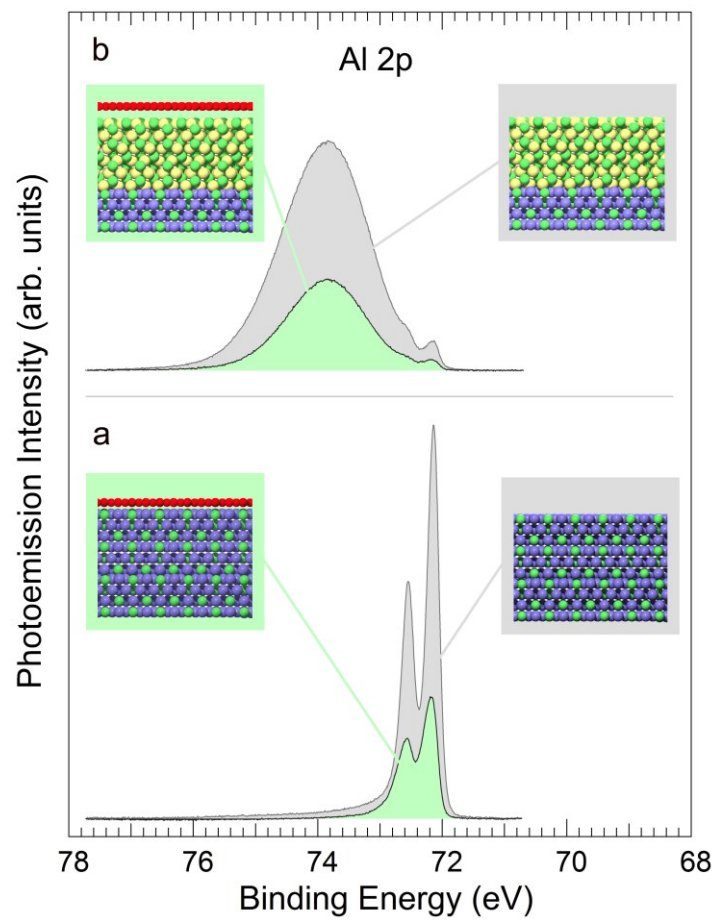


**Figure 4 | Alumina layer properties: clean vs GR covered sample.** Al 2p photoemission spectra acquired in similar condition for the clean (gray) and GR covered (green) sample: **(a)** clean substrate, and **(b)** after formation of an alumina nanosheet.